DRAFT VERSION OCTOBER 16, 2015
Preprint typeset using LaTeX style emulateapj v. 5/2/11

arXiv:1410.0039v3 [astro-ph.HE] 14 Oct 2015

EMISSION FROM PAIR-INSTABILITY SUPERNOVAE WITH ROTATION

E. CHATZOPOULOS[1,7], VAN ROSSUM, DANIEL R.[1], WHEELER, J. CRAIG [2], DANIEL J. WHALEN[3], JOSEPH SMIDT[4] & BRANDON WIGGINS[5,6]

Draft version October 16, 2015

ABSTRACT

Pair Instability Supernovae have been suggested as candidates for some Super Luminous Supernovae, such as SN 2007bi, and as one of the dominant types of explosion occurring in the early Universe from massive, zero-metallicity Population III stars. The progenitors of such events can be rapidly rotating, therefore exhibiting different evolutionary properties due to the effects of rotationally-induced mixing and mass–loss. Proper identification of such events requires rigorous radiation hydrodynamics and radiative transfer calculations that capture not only the behavior of the light curve but also the spectral evolution of these events. We present radiation hydrodynamics and radiation transport calculations for 90-300 $M_{\odot}$ rotating pair-instability supernovae covering both the shock break-out and late light curve phases. We also investigate cases of different initial metallicity and rotation rate to determine the impact of these parameters on the detailed spectral characteristics of these events. In agreement with recent results on non-rotating pair instability supernovae, we find that for a range of progenitor masses and rotation rates these events have intrinsically red colors in contradiction with observations of super-luminous supernovae. The spectroscopic properties of rotating pair instability supernovae are similar to those of non-rotating events with stripped hydrogen and helium envelopes. We find that the progenitor metallicity and rotation rate properties are erased after the explosion and cannot be identified in the resulting model spectra. It is the combined effects of pre-supernova mass–loss and the basic properties of the supernova ejecta such as mass, temperature and velocity that have the most direct impact in the model spectra of pair instability supernovae.

Subject headings: physical data and processes: radiative transfer — stars: rotation — stars: massive — supernovae: general, supernovae: individual (pair-instability)

1. INTRODUCTION

The importance of understanding the supernova (SN) explosions of very massive stars ($M_{\rm ZAMS} > 50\ M_{\odot}$) is pertinent in both low and high redshift. Recent developments in transient astrophysics led to the discovery of a new class of relatively nearby ($z \sim 0$ - 1.2) explosions with peak luminosities ∼10-100 greater than those of all types of core-collapse supernova (CCSN) events and with a striking degree of diversity in their emission properties, the superluminous supernova (SLSN) events (Quimby et al. 2007; Smith et al. 2007, see also Gal-Yam 2012 for a review and more references).

Although the extreme luminosities of the majority of the observed SLSNe are attributable to other processes, such as strong SN ejecta - circumstellar matter (CSM) interaction (Smith & McCray 2007; Chatzopoulos et al. 2011; Chatzopoulos & Wheeler 2012b; Moriya & Tominaga 2012; Moriya et al. 2013; Chatzopoulos et al. 2013b; Benetti et al. 2014; Nicholl et al. 2014) or efficiently thermalized proto-magnetar spin-down radiation (Kasen & Bildsten 2010; Woosley 2010; Dessart et al. 2012; Lunnan et al. 2014; McCrum et al. 2014), there are still a few SLSN light curves (LCs) that seem to be well fit by explosions of very massive progenitor stars ($M_{\rm ZAMS} > 130\ M_{\odot}$) powered by the radioactive decay of large amounts of ^{56}Ni ($M_{\rm Ni} >$ 1-10 $M_{\odot}$, Heger & Woosley 2002; Woosley et al. 2007) with the most well-studied case being SN 2007bi (Gal-Yam et al. 2009; Gal-Yam 2012; Kasen et al. 2011; Kozyreva et al. 2014; **?**).

These pair-instability supernovae (PISNe; Rakavy & Shaviv 1967; Barkat et al. 1967; Rakavy et al. 1967; Ober et al. 1983; Heger & Woosley 2002; Chatzopoulos & Wheeler 2012a; Chatzopoulos et al. 2013a; Yusof et al. 2013; Chen et al. 2014a,b) occur when the helium cores of very massive stars enter a regime of high temperature ($\gtrsim 10^9$ K) and relatively low density ($\sim 10^3$-10^6 g cm^{-3}) allowing rapid production of electron-positron (e^--e^+) pairs ($M_{\rm ZAMS} \simeq$ 130-260 $M_{\odot}$, $M_{\rm CO} \simeq$ 60-140 $M_{\odot}$ for non-rotating progenitors at ZAMS, where $M_{\rm CO}$ is the mass of the He core; Heger & Woosley 2002; Woosley et al. 2007). Note that we use the "CO" notation since 75% of the He core is, in reality, C and O. The rapid electron-positron pair production leads to the reduction of radiation pressure in the core and the decrease of the adiabatic index, Γ_{ad}, below 4/3 resulting in core contraction and, consequently explosive nuclear burning and the production of a strong SN shock that totally disrupts the star.

A few very massive stars (VMS) that seem to fit the criteria to be PISN progenitors have been discovered (Crowther et al. 2010). At near to solar metallicities, models predict that the effects of radiatively-driven mass–loss are so strong that they can drive the mass of the star below the range required for PISNe (Langer et al. 2007; but see Kozyreva et al. 2014 for an alternative view). In fact, the measured metallicities of most SLSN hosts are always larger than $\sim 0.1\ Z_{\odot}$ (Stoll et al.

manolis@flash.uchicago.edu
[1] Department of Astronomy & Astrophysics, Flash Center for Computational Science, University of Chicago, Chicago, IL, 60637, USA
[2] Department of Astronomy, University of Texas at Austin, Austin, TX, 78712, USA
[3] Universität Heidelberg, Zentrum für Astronomie, Institut für Theoretische Astrophysik, Albert-Ueberle-Str. 2, 69120 Heidelberg, Germany
[4] T-2, Los Alamos National Laboratory, Los Alamos, NM 87545, USA
[5] CCS-2, Los Alamos National Laboratory, Los Alamos, NM 87545, USA
[6] Department of Physics and Astronomy, Brigham Young University, Provo, UT 84602
[7] Enrico Fermi Fellow

2013; Lunnan et al. 2014).

The prevalence of PISNe is therefore expected to be higher in very low to zero metallicity environments characteristic of the conditions in the early Universe. The Population III stars are found to be quite massive in primordial star formation simulations, well in the PISN regime (Abel et al. 1998; Bromm et al. 2002; Bromm & Larson 2004; Stacy et al. 2012, 2013). Pending the deployment of future missions such as the *James Webb Space Telescope* (*JWST*) and the *Wide Field Infrared Survey Telescope* (*WFIRST*), it has been broadly proposed to look for the primordial PISNe explosions resulting from the first stars (Scannapieco et al. 2005; Bromm et al. 2009; Joggerst & Whalen 2011; Pan et al. 2012; Hummel et al. 2012; Whalen et al. 2013b,a; Glover 2013; Whalen 2013; de Souza et al. 2014).

Since PISNe can be linked to both SLSNe and primordial Pop III SNe, it is critical to understand their radiative properties across the relevant parameter space. So far the corresponding efforts have focused on non-rotating PISN progenitors on the high end of the mass range. Gray flux limited diffusion (FLD) radiation hydrodynamics model LCs have been presented in the context of the detectability of primordial PISNe (Scannapieco et al. 2005; Whalen et al. 2013b,a) but also to compare to the observed LCs of some SLSNe such as SN 2006gy (Woosley et al. 2007) and SN 2007bi and PTF10nmn (Gal-Yam et al. 2009; Kasen et al. 2011; Kozyreva et al. 2014; **?**).

A rigorous, self-consistent comparison with observed SN spectra requires accurate modeling of the observed spectral evolution and not just the bolometric and broad band LCs. Dessart et al. (2013) demonstrated this fact by non local thermal equillibrium (non–LTE) radiative transfer calculations yielding model non-rotating PISN spectra as a function of time with the *CMFGEN* code (Hillier & Dessart 2012). They found that PISNe are intrinsically too red in color as compared to SLSN events like SN 2007bi, and that their spectral evolution does not match that of any observed SN so far.

Recently, it has been shown that the inclusion of the effects of rotation in the evolution of PISN progenitors changes some key characteristics of these events (Chatzopoulos & Wheeler 2012b,a; Yoon et al. 2012; Chatzopoulos et al. 2013a). More specifically, rotationally–induced mixing can shift the mass limit to encounter PISN to lower values (85 $M_{\odot} < M_{\rm ZAMS} < 190\ M_{\odot}$ at rotation rates 50 % that of the critical Keplerian value). In addition, the combined effects of mixing and rotationally–induced mass–loss often lead to bare CO cores (stripped totally of both H and He) prior to explosion and to differences in mixing, ^{56}Ni yields, and energetics, therefore changing the interplay between energy input and SN ejecta opacity. This alone may have an effect on the radiative properties of these events as compared to non-rotating PISNe.

Rapid stellar rotation has been observed for some massive nearby stars (Dufton et al. 2011) and it is also found in simulations of primordial massive star formation (Greif et al. 2011; Stacy et al. 2013). To further complement the parameter space relevant to PISN explosions, in this work we present radiation hydrodynamics and LTE radiative transfer calculations of PISNe resulting from rotating progenitors and compare our results to the non-rotating case and to some observed SNe and the PISN candidate SN 2007bi.

The paper is organized as follows. In Section 2 we present the 1D stellar evolution and hydrodynamics simulations of rotating PISN progenitors up to a time prior to shock break out (SBO). In Section 3 we discuss the shock break out emission using results from radiation hydrodynamics simulations. In Section 4 we present LTE LCs and spectra of rotating PISNe and compare with results from non-rotating models (Kasen et al. 2011; Dessart et al. 2013) as well as observations of SLSNe like SN 2007bi and other events. Lastly, in Section 5 we summarize and discuss our conclusions.

2. STELLAR EVOLUTION AND HYDRODYNAMICS SIMULATIONS

In order to obtain time-dependent spectra and final LCs for rotating PISNe, we followed a multi-step process. First we evolved a grid of progenitors from the Zero Age Main Sequence (ZAMS) up to the point when the dynamical instability is encountered using the stellar evolution code Modules for Experiments in Stellar Astrophysics (*MESA*; Paxton et al. 2011, 2013). At this point, the structure of the star was becoming dynamical and the semi-hydrostatic stellar evolution code reached its limitations. For this reason, we conservatively mapped the *MESA* models to the 1D Adaptive Mesh Refinement (AMR) grid of the multi-physics hydrodynamics code *FLASH* (Fryxell et al. 2000; Dubey et al. 2009) and followed the evolution of the explosion up to the epoch before SN SBO. Since we needed to capture the full radiation hydrodynamics nature of SN SBO involving the separation of matter and radiation temperatures, the next step involved re-mapping of the blast profiles to the radiation hydrodynamics code *RAGE* (Gittings et al. 2008; Frey et al. 2013). The *RAGE* profiles were post-processed by the Los Alamos National Lab (LANL) *SPECTRUM* (Frey et al. 2013) code yielding SBO LCs and spectra. Finally, once the SN ejecta were expanding homologously the post-SBO profiles were mapped in the Langrangian grid of the radiative transfer code *PHOENIX* (Hauschildt 1992; Hauschildt & Baron 1999, 2004; van Rossum 2012a) that provided us with time-dependent spectra and LCs of rotating PISNe. We only calculated SBO LCs for 10 zero metallicity rotating models because PISN models of higher metallicity and zero rotation have already been investigated (Kasen et al. 2011; Dessart et al. 2013).

2.1. *MESA pre-supernova evolution.*

We modeled the evolution of 10 PISN progenitor stars with zero initial ZAMS metallicity, rotation at 50% that of the critical Keplerian value at the equator and in the mass range 90-140 $M_{\odot}$ using *MESA* version 5596. This mass range was motivated by the finding of Chatzopoulos & Wheeler (2012a) and Yoon et al. (2012) that full-fledged zero metallicity PISNe that rotate with $\Omega/\Omega_{\rm c,ZAMS} = 0.5$ occur for ZAMS masses $> 85\ M_{\odot}$. In the above expression, Ω and $\Omega_{\rm c,ZAMS}$ are the angular velocity at the equator and the critical value of angular velocity at ZAMS, respectively.

The zero metallicity models were considered because of their relevance to primordial star formation and the proposals to look for the PISN explosions from the first massive stars (Scannapieco et al. 2005; Whalen et al. 2013b,a). For that same reason, we adopted an initial rotation rate of $\Omega/\Omega_{c,ZAMS} = 0.5$ that seems to be a characteristic value found in early Universe star formation simulations (Greif et al. 2011; Stacy et al. 2013).

In order to properly assess the parameter space, but also to study models relevant to nearby recently discovered PISN candidates such as SN 2007bi, we calculated two rotating PISN models at higher metallicities (260 $M_{\odot}$ at

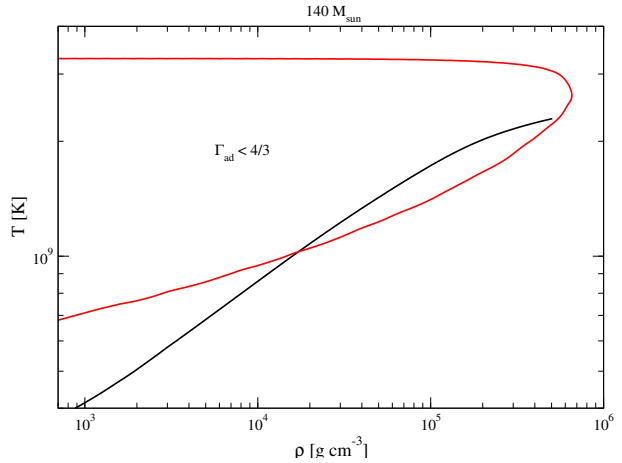

Figure 1. The black curve shows the nitial *MESA* progenitor ρ-T profile for the 140 $M_\odot$ model prior to mapping to the grid of *FLASH*. The thick red curve denotes the region where $\Gamma_{ad} < 4/3$ due to the effects of e^-- e^+ pair production.

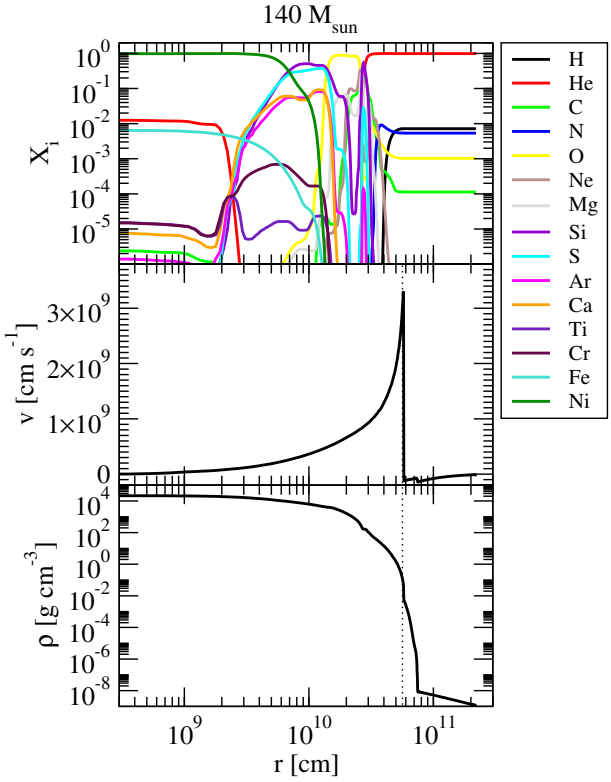

Figure 2. 1D *FLASH* radial profiles of composition (upper panel), velocity (middle panel) and density (lower panel) for the 140 $M_\odot$ model prior to mapping to the grid of *RAGE* just before SN shock break-out. The dotted vertical lines correspond to the location of the SN shock.

0.05 $Z_\odot$ and 300 $M_\odot$ at 0.1 $Z_\odot$ at the ZAMS both with $\Omega/\Omega_{\rm c,ZAMS} = 0.5$). These large ZAMS masses are characteristic of the most massive stars observed (Crowther et al. 2010). Very large ZAMS mass is required in order to counter the strong effects of radiatively-driven mass-loss at these high metallicities allowing the formation of final cores with masses in the PISN regime. To determine whether the presence of metals in otherwise identical PISNe can be detected in model spectra, we artificially added metal content in the 140 $M_\odot$ model assuming $Z = 0.1$ $Z_\odot$ prior to mapping to *PHOENIX* and re-normalized all the abundances ("pP" model). In addition, to determine whether the presence of the same metal content in the 140 $M_\odot$ model has an effect on the explosive PISN nucleosynthesis we also added the same metal content (0.1 $Z_\odot$) prior to mapping to *FLASH* ("pF" model). Although the models with artificially added metallicity ("pP" and "pF") are not entirely self-consistent since the presence of metals will itself change the pre-SN evolution, we use these models to gain intuition on the magnitude of the effect.

Finally, to probe spectroscopic differences that might arise due to varying degrees of pre-PISN rotation rate, we calculated two zero metallicity non-rotating models (with $M_{\rm ZAMS} = 200$ and 260 $M_\odot$) and a 140 $M_\odot$ model with $\Omega/\Omega_{\rm c,ZAMS} = 0.5$ but without the effects of mixing and angular momentum transport due to the magnetic fields by turning off the Spruit-Taylor (ST) mechanism (140 $M_\odot$ "no-ST" model). The absence of magnetic viscosity in this model led to a much faster rotating pre-PISN core ($\Omega/\Omega_{\rm c} \simeq 0.3$). As a result we calculated a total of four 140 $M_\odot$ models spanning the rotation and metallicity parameter space: the original model with the effects of ST included, one without the effects of ST and two with artifically added metallicity (0.1 $Z_\odot$) prior to doing the PISN nucleosynthesis in *FLASH* and prior to mapping to *PHOENIX* to calculate the radiative transfer properties. For details on the *MESA* parameters used (equation of state, nuclear reaction network, resolution, treatment of mass–loss and rotation) refer to Chatzopoulos & Wheeler (2012a). The basic properties of the PISN models we examine in this work are listed in Table 1.

The effects of rotation and magnetic fields via the ST mechanism (Spruit 1999, 2002) on the evolution of massive stars have been investigated thoroughly in the past with the use of different stellar evolution codes (Heger et al. 2000; Yoon & Langer 2005; Brott et al. 2011a,b; Ekström et al. 2008, 2012; Chatzopoulos & Wheeler 2012b; Yoon et al. 2012), also see (Maeder & Meynet 2011) for a review. Enhanced chemical mixing, primarily due to meridional circulation and the ST mechanism, can lead to the formation of more massive CO cores for a lower ZAMS mass than required in the case of zero rotation. Furthermore, diffusion of angular momentum can lead to additional, mechanically-induced mass–loss (Heger et al. 2000) that in turn can, under some circumstances, result in the stripping of both the H and He envelopes from the SN progenitor star leaving a bare CO core remnant.

This is the case for most of the models we consider in this work. In particular, we stopped the *MESA* calculations when a significant portion of the pre-PISN CO cores was in the pair-instability regime of $\Gamma_{\rm ad} < 4/3$ and the model was becoming dynamical. In general this was the phase of core carbon exhaustion, in agreement with (Dessart et al. 2013). Figure 1 shows the temperature-density (ρ-T) structure of the 140 $M_\odot$ model when the *MESA* run was interrupted. Note that a significant portion of the model lies within the pair-instability regime marked by the thick red curve.

For all of the models considered here the final, pre–SN mass of the CO core remnants ($M_{\rm CO}$) was in the range of $\sim$ 60-112 $M_\odot$ and the final radius, $R_{\rm f}$, in the range 4×10^{10}-4×10^{13} cm. The rotating models consintently made more compact PISN progenitors due to the effects rotationally-enhanced mass-loss. Due to angular momentum transport

during the main evolution, the final, pre–SN rotation rates of the CO cores were somewhat modest ($\Omega/\Omega_c \simeq 0.02$-$0.06$) with the exception of the 140 $M_\odot$ no-ST model. As such, most of these pre–SN models have somewhat different structural properties than other PISN models considered so far in the literature for radiative transfer studies (Gal-Yam et al. 2009; Kasen et al. 2011; Dessart et al. 2013). They are compact, well chemically-mixed slowly rotating CO stars with the H envelope removed in all cases and with a low, even zero in a few cases, He envelope mass.

2.2. *1-D FLASH hydrodynamics.*

All the pre–SN 1D profiles from *MESA* were mapped to the 1D AMR Eulerian grid of *FLASH*-4.0 (Fryxell et al. 2000; Dubey et al. 2009). The same basic physics units (equation of state, nuclear reaction network) are used in *FLASH* as in the *MESA* stellar evolution calculations with the exception that we did not map the pre–SN rotational profile for the hydrodynamics simulation. As Chatzopoulos et al. (2013a) have shown, when the magnetic viscosity and angular momentum transport due to the ST dynamo action are included in the stellar evolution calculation, the pre–SN rotation is slow and does not affect the final hydrodynamics. It is the pre–SN mixing changing the structure of the progenitor star and the composition gradient effects that primarily determine the final dynamics and nucleosynthetic properties of the explosion. Also, the oblateness of the star due to rotation will be negligible for the moderate pre–SN rotational velocities of our suite of models.

We follow the collapse, explosion and nucleosynthesis in *FLASH* up until prior to SN SBO, that we take to be the phase when the SN shock is within a hundred to a few thousand optical depths from the surface of the star, still in the optically thick regime. We recall that $\tau_{\rm SBO} = c/v_{\rm sh}$ where $\tau_{\rm SBO}$ is the SBO optical depth, $v_{\rm sh}$ the velocity of the SN shock (typically of the order of a few 10^9 cm s^{-1}) and c the speed of light. Figure 2 shows the composition (upper panel), velocity (middle panel) and density (lower panel) for the pre-SBO stage when we halt the *FLASH* simulation in the case of the 140 $M_\odot$ model. As illustrated in Figure 2, the basic structure of this model consists of ^{56}Ni located in the base of H-poor SN ejecta. Table 1 details the basic characteristics of all PISN explosion models. Our set of models produced final ^{56}Ni masses in the range 0.1-22 $M_\odot$ embedded in SN ejecta of 60-112 $M_\odot$. The $M_{\rm Ni}/M_{\rm f}$ ratios for our rotating 90-140 $M_\odot$ and non-rotating 200 $M_\odot$ and 260 $M_\odot$ PISN models are consistent with those of Dessart et al. (2013) meaning that, modulo differences in SN ejecta opacity, our models are expected to manifest as dimmer events (in terms of bolometric LC) that have rather red colors. We test this prediction in Section 4.

3. ROTATING PISN SHOCK BREAKOUT EMISSION

As an intermediate step, the 10 final rotating zero metallicity PISN *FLASH* profiles were mapped into the 1D AMR Eulerian grid of the radiation hydrodynamics code *RAGE* (Gittings et al. 2008; Frey et al. 2013) where the emission during the SBO phase is modeled. We did not map the other models into *RAGE* because higher metallicity and non-rotating PISN SBO properties have already been well studied in the literature (Whalen et al. 2013b,a). The SBO LCs are calculated by post-processing the *RAGE* snapshots with the LANL code *SPECTRUM* (Frey et al. 2013). For details on the physics, resolution and other parameters used in *RAGE* and *SPECTRUM* please see Whalen et al. (2013b).

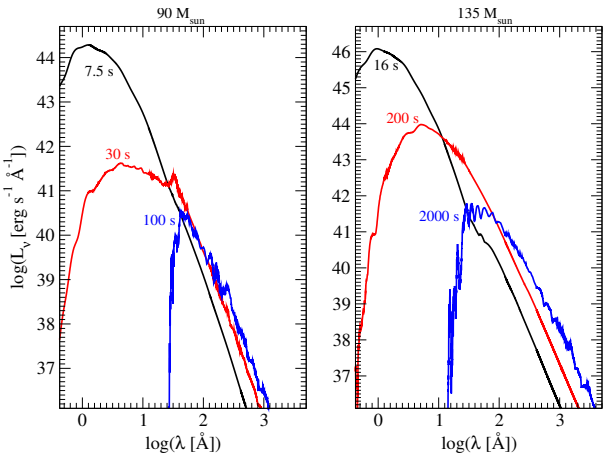

Figure 3. Post-SBO SED evolution for the 90 $M_\odot$ (left panel) and the 135 $M_\odot$ (right panel) model as calculated by *SPECTRUM*. The SED phases are shown on top of the corresponding curves. The SBO emission for a bare CO rotating PISNe peaks in the hard X-rays (0.1-10 Å or $\sim$ 1-100 keV).

The *RAGE* and *SPECTRUM* results on the ^{56}Ni radioactive decay powered re-brightening seem to conflict with earlier results and a code comparison effort is underway to determine the source of this discrepancy (Whalen et al. 2013a). Possible sources include differences in opacities, resolution and the issue of what fraction of the radioactive decay energy goes into increasing the kinetic energy of the inner SN ejecta versus pure radiative losses. Homologous LTE and non–LTE codes are engineered to predict behavior closer to the latter while *RAGE* radiation hydrodynamics favors the former case. In this paper, we are only using *RAGE* to model the SBO emission during the first few days of radiation hydrodynamical evolution while for the later evolution (homologous expansion phase) we use the LTE treatment of the *PHOENIX* code (Section 4).

The SBO LCs have some dependence on the properties of the CSM that is superimposed on the SN blast profiles in the *RAGE* grid. For the purposes of this study, the abrupt density gradient between the edge of the star and the wind is bridged by an r^{-20} profile to minimize effects of numerical instabilities during the SBO phase. Then the wind profile follows an inverse square power-law given explicitly by $\rho_w = \dot{M}/(4\pi v_w r^2)$ where ρ_w is the wind density, $\dot{M}$ the wind mass–loss rate and v_w the wind velocity taken to be 1000 km s^{-1}. For all models we fix the density at the bottom of the wind profile to be $\sim 2 \times 10^{-18}$ g cm^{-3} so that the CSM is optically thin.

Using *SPECTRUM*, the spectral energy distributions (SEDs) during the first few days after SBO are calculated and then integrated yielding the final bolometric LCs. In Figure 3 the first few minutes of post-SBO SED evolution for the 90 $M_\odot$ and the 135 $M_\odot$ models are shown. The SBO spectra for all of our models exhibit a characteristic "expanding fireball" behavior that is well described by a cooling black body continuum with some spectral lines superimposed, especially during the later phases. The peak of the emission during SBO is in the hard X-ray part of the spectrum (0.1-10 Å or $\sim$ 1-100 keV) at significantly shorter wavelengths than SBO emission from red supergiant (RSG) and blue supergiant (BSG) PISN progenitors (Kasen et al. 2011).

Figure 4 shows the resulting SBO bolometric LCs (solid

Table 1
Properties of PISN progenitor models.

$M_{\rm ZAMS}$ ($M_\odot$)	$Z_{\rm ZAMS}$ ($Z_\odot$)	$R_{\rm f}$ (10^{10} cm)	$M_{\rm f}$ ($M_\odot$)	$M^{\dagger}_{\rm CO}$ ($M_\odot$)	$M_{\rm Ni}$ ($M_\odot$)	$E_{\rm SN} - E_{\rm b,f}{}^{*}$ (10^{52} erg)	$M_{\rm bol,peak}$ (mag)
90	0.0	3.925	60.51	59.31	0.138	0.98	-16.08
95	0.0	5.598	68.97	63.48	0.327	1.07	-16.93
105	0.0	4.730	71.12	69.10	0.853	2.84	-17.96
110	0.0	5.707	74.93	70.35	1.141	3.94	-18.15
115	0.0	8.266	76.73	70.48	1.070	3.12	-18.05
120	0.0	6.565	79.03	72.57	1.565	4.28	-18.52
125	0.0	8.034	83.60	76.80	3.255	5.04	-19.30
130	0.0	10.616	85.64	77.69	3.870	5.23	-19.47
135	0.0	18.324	90.15	79.76	4.521	6.16	-19.66
140	0.0	7.649	91.30	83.71	7.297	7.95	-20.24
140pF	0.1	7.649	91.30	85.60	6.453	7.62	-20.24
140pP	0.1	7.649	91.30	83.71	7.297	7.95	-20.24
140no-ST	0.0	22.341	91.82	85.17	2.489	3.08	-19.20
200[a]	0.0	3772.167	111.28	82.48	0.165	1.55	-16.00
260[a]	0.0	1398.403	139.43	95.11	9.858	4.94	-20.50
260	0.05	7.299	116.85	112.02	22.22	6.64	-21.50
300	0.1	9.322	111.02	111.02	12.70	4.78	-20.92

Note. — † $M_{\rm CO}$ is the mass of the carbon-oxygen core defined as the total mass within the radius where $X_{\rm C} + X_{\rm O} > 0.5$. * The nuclear energy released by the SN explosion, $E_{\rm SN}$, minus the pre-SN binding energy of the progenitor, $E_{\rm b,f}$. [a] These models were evolved without rotation.

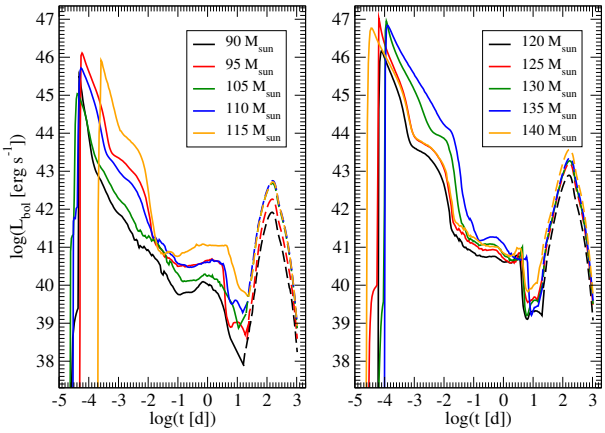

Figure 4. *RAGE/SPECTRUM* SBO (solid curves) and *PHOENIX* late-time (dashed curves) LCs for the grid of rotating PISNe models studied here. *Left Panel*: 90-115 $M_\odot$. *Right Panel*: 120-140 $M_\odot$.

curves) for all of the models discussed in this paper. The late-time *PHOENIX* LCs are also shown (dashed curves) for completeness but discussed in detail in Section 4. The peak SBO luminosities for all models are in the range 10^{45}-10^{46} erg s^{-1} and are consistent with the Kasen et al. (2011) results despite the different progenitor properties. This is mainly because although our post-SBO temperatures and velocities are higher and the emission peaks at lower wavelengths, the radii of our progenitor models are smaller than both the RSG and BSG series presented in Kasen et al. (2011). The rotating PISN SBO bursts are also found to be close in terms of duration with those for BSG progenitors in Kasen et al. (2011). After the end of the SBO bursts (0.01-0.1 days), the luminosities are mainly driven by hydrodynamical effects (reverse and forward shock heating) before the much longer re-brightening phase due to the radioactive decays of ^{56}Ni and ^{56}Co starts.

4. TIME-DEPENDENT RADIATIVE TRANSFER

In order to calculate time-dependent model spectra for our rotating PISN models we first converted the blast profiles from *FLASH* at 1 hr after SBO into the Langragian grid using velocity as the independent variable. These profiles are then input to the radiative transfer code *PHOENIX* (Hauschildt 1992; Hauschildt & Baron 1999, 2004; van Rossum 2012a), allowing us to retrieve model light curves, color and spectral evolution.

At first, it might seem questionable that we elected to use the *FLASH* post-SBO profiles instead of the *RAGE* ones that properly model the radiation hydrodynamic effects during that early phase; however, once the SBO effects have ceased we find that the density and mass fraction profiles calculated by the two codes are almost identical up to $\sim$ 1-4 days, depending on the model. To illustrate this we present the Lagrangian density profiles for the 140 $M_\odot$ model at 1 hr in Figure 5 for both *FLASH* (black curve) and *RAGE* (red curve). We have verified that the resulting final model LCs and spectra are virtually invariable with respect to what input profile is used at 1 hr after SBO (*FLASH* or *RAGE*).

PHOENIX solves the special relativistic radiative transfer problem in spherical symmetry using the highly accurate short characteristics and and operator splitting methods (Olson & Kunasz 1987). The time-evolution of the post-hydrodynamic, radiation-dominated phase is followed using the Radiation Energy Balance method (van Rossum 2012a). *PHOENIX* does not use the Sobolev approximation, diffusion approximations, or opacity binning. The deterministic nature of the radiative transfer method enables calculation of noise-free spectra, a feature which enables us to show detailed line identifications for the presented model spectra (see next paragraph).

4.1. *Zero metallicity 90-140 $M_\odot$ PISNe.*

The spectral evolution of the lower mass (90 $M_\odot$) and the higher mass (140 $M_\odot$) rotating PISN is shown in Figure 6, where the phases cited are with respect to the time of peak luminosity during the later phase of ^{56}Ni heating of the ejecta. The hotter, more massive models are less line-dominated than the less massive ones and exhibit a stronger continuum due

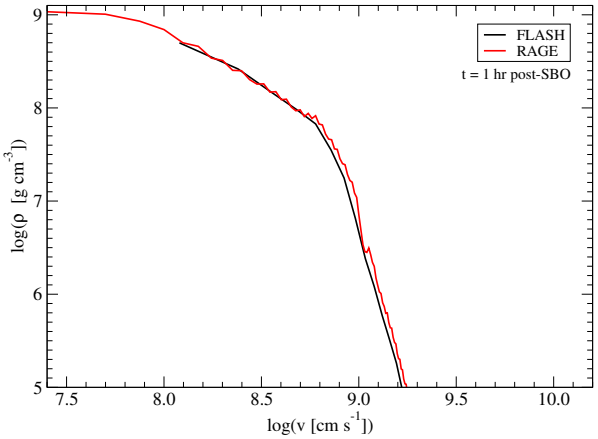

Figure 5. Scaled density profile in Lagrangian coordinates at 1 hr after SBO in *FLASH* (black curve) and *RAGE* (red curve). It can be seen that the pure hydrodynamics and radiation hydrodynamics profiles are in good agreement shortly after SBO as discussed in § 4.

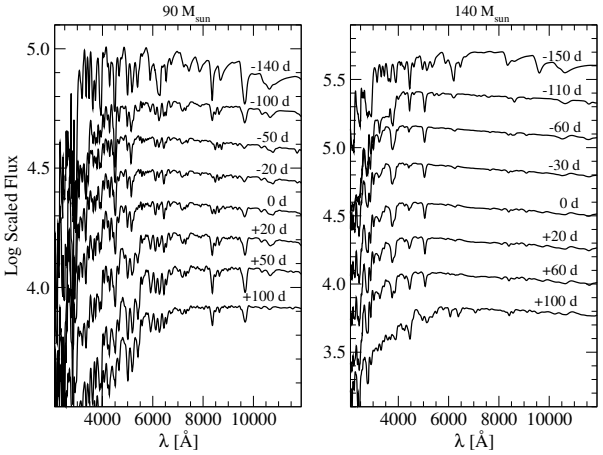

Figure 6. *PHOENIX* spectral evolution for the 90 $M_{\odot}$ (left panel) and the 140 $M_{\odot}$ (right panel) models. The phases are shown with respect to the time of ^{56}Ni decay peak luminosity.

to their higher temperatures. To better illustrate the spectroscopic characteristics of rotating PISNe we also show only the peak luminosity spectra for all models in Figure 7 as well as detailed spectral line identifications in Figure 8 for the 90 and 140 $M_{\odot}$ models.

The spectral line identification shown in Figure 8 was performed by removing the line-opacity from individual ions, rerunning the *PHOENIX* models and comparing with the original spectrum. The difference between each of the "knock-out" spectra and the original is attributed to the lines of the respective ion (van Rossum 2012b). In Figure 8 we stack the differences in flux level from different runs on top of each other, using distinct colors for different chemical elements. Colored patches on top of the original flux level are caused by (the absence of) absorption, and patches below the original flux level by (the absence of) emission. The plots show that some of the lines that appear in the spectra can not be fully attributed to a single chemical element but rather to a combined effect of multiple species.

Figures 6 through 8 reveal that the optical spectra of all rotating PISN spectra are dominated by Intermediate Mass Elements (IMEs). More specifically, the early to peak luminosity spectra are dominated by strong Mg, Si, and Ca lines with some iron-group elements present in the near-UV (mostly Cr and Ti). The strong Mg absorption is due to the high abundance of Mg in the middle layer of the PISN ejecta (for example see the upper panel of Figure 2). Enhanced Mg in PISN ejecta is also seen by other studies (Heger & Woosley 2002; Woosley et al. 2007) and it is the result of the passage of the burning flame from this region before it shuts off prior to reaching the outer ejecta. The 6000 Å $< \lambda <$ 8000 Å domain is virtually devoid of prominent line features in the more massive model (with the exception of the Si λ6150 Å). In addition, all models show prominent Si absorption features in the near-IR ($\lambda >$10500 Å).

Although the SN ejecta had considerable amounts of He, no significant He features are seen in any of the spectra due to the fact that the photosphere recedes quickly through the He envelope but also due to the low envelope temperatures that are insufficient for low atomic level excitation and generation of optical lines. We caution, however, that non–LTE treatment

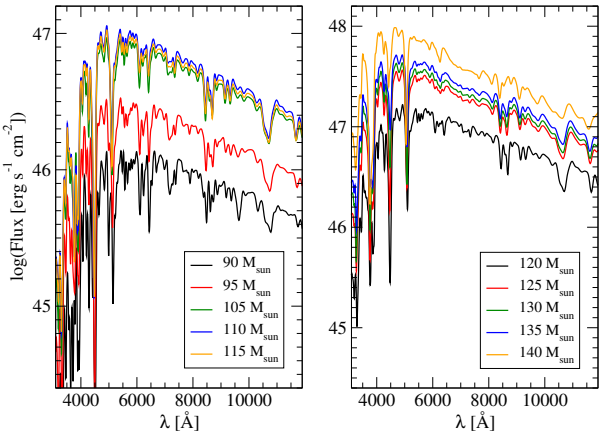

Figure 7. *PHOENIX* spectra at peak luminosity for the zero metallicity rotating 90-140 $M_{\odot}$ PISNe. *Left Panel*: 90-115 $M_{\odot}$. *Right Panel*: 120-140 $M_{\odot}$.

will likely result in the presence of some He features due to excitation by secondary electrons produced by Compton scattering of the gamma rays produced by the radioactive decays of ^{56}Ni and ^{56}Co (Lucy 1991; Hachinger et al. 2013). Over time as the expanding SN ejecta cool and the photosphere recedes into the inner regions additional lines appear characteristic of the inner ejecta (Ti, Cr, Fe, Co; bottom panels of Figure 8). The basic spectral characteristics are very similar to those observed in the He100 models of Kasen et al. (2011) and Dessart et al. (2013).

Convolution of the spectra with the standard *UBVRIJHK* broad-band filters allows for the calculation of photometric LCs that are shown in Figure 9 for the 90 $M_{\odot}$ and the 140 $M_{\odot}$ models. In a manner characteristic of regular SN events, the redder LCs are brighter and with longer diffusion time-scales. Integration of the spectra yields the final bolometric LCs for all of the rotating PISN models studied here, shown in Figure 10. The peak bolometric luminosities are in the range 10^{43} -5 $\times$ 10^{44} (corresponding to bolometric magnitudes in the range -16 $\lesssim M_{\rm bol} \lesssim$ -20) while the rise time to peak luminosity is in the range 140-170 d in all cases. As such, none of

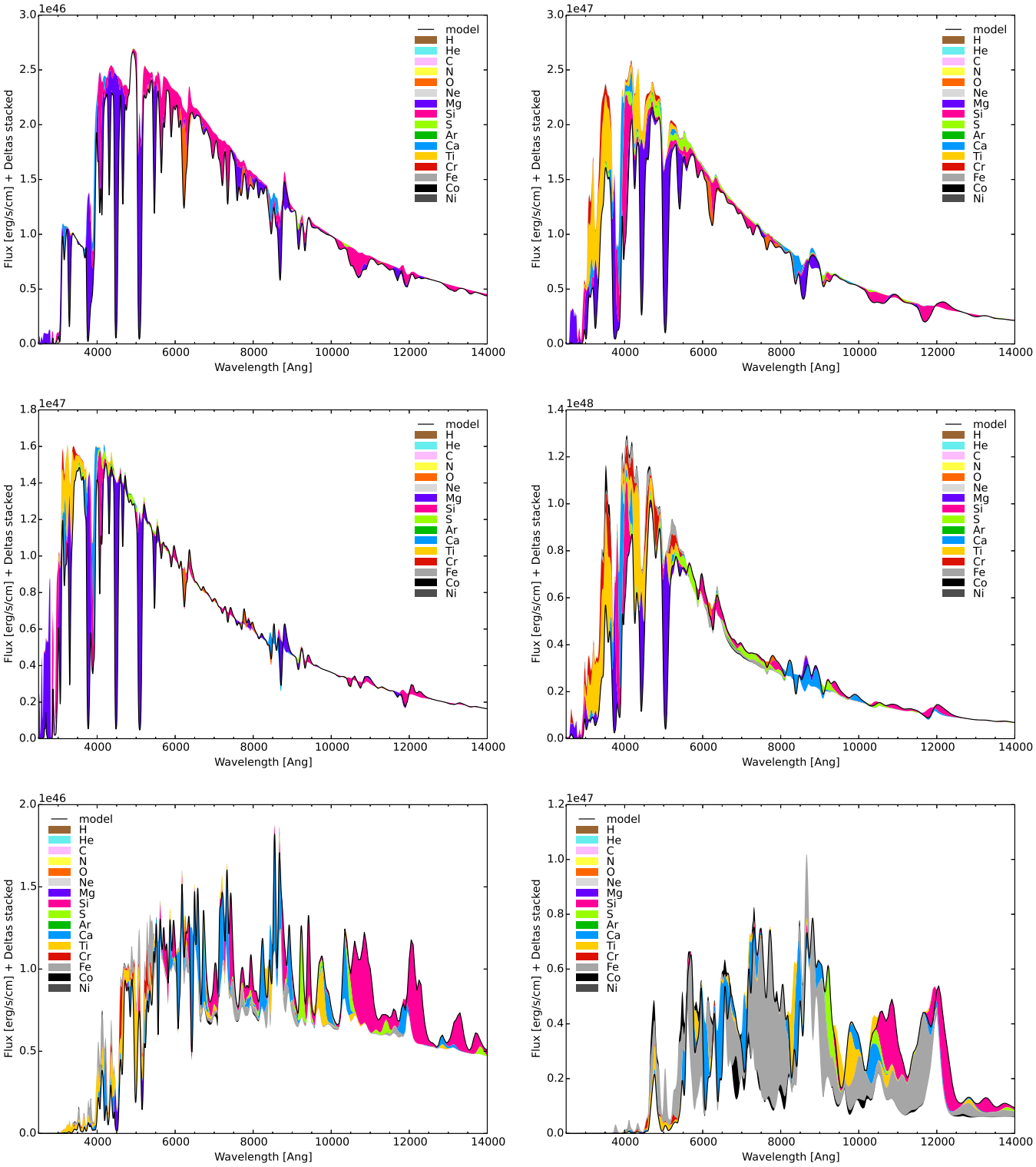

Figure 8. *PHOENIX* spectral line identification for the 90 $M_\odot$ model (left panels; -64 d, 0 and 204 d with respect to peak luminosity from top to bottom) and the 140 $M_\odot$ panel (right panels; -84 d, 0 and 184 d with respect to peak luminosity from top to bottom). The thick black curve is the original full spectrum. For a more detailed interpretation of this plot refer to the discussion in § 4.1.

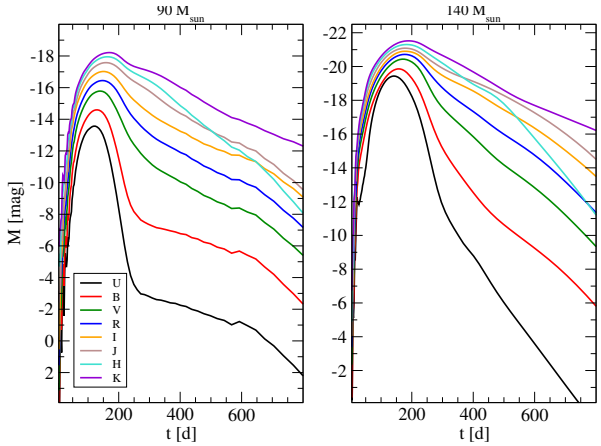

Figure 9. Broad-band *UBVRIJHK PHOENIX* LCs for the 90 $M_{\odot}$ (left panel) and the 140 $M_{\odot}$ (right panel) models. Note how the SN LC is dimmer and has a steeper post-maximum decline in shorter wavelengths.

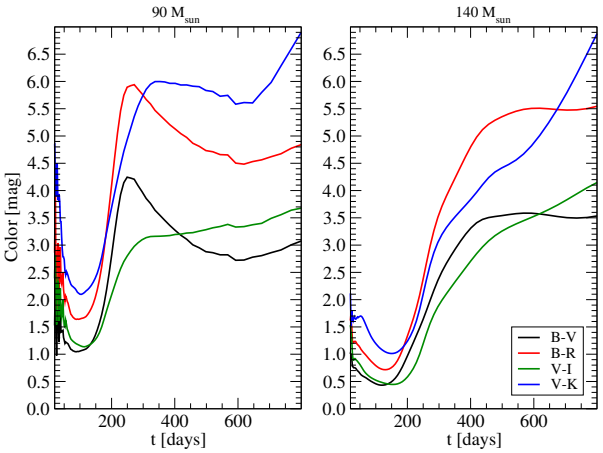

Figure 11. Evolution of the $B-V$, $B-R$, $V-I$ and $V-K$ colors for the 90 $M_{\odot}$ (left panel) and the 140 $M_{\odot}$ (right panel) model. The color evolution of PISNe is redder than that of other types of SNe.

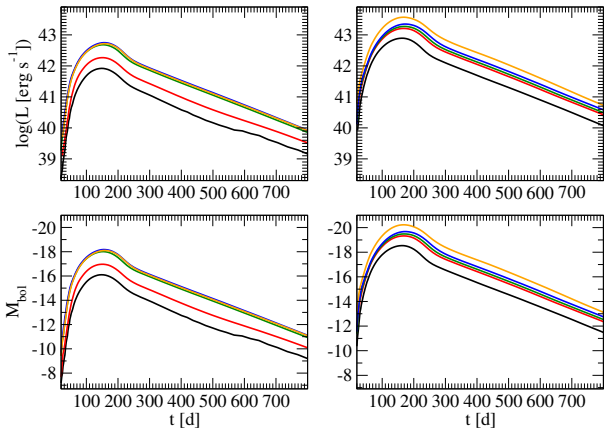

Figure 10. *PHOENIX* LCs in terms of luminosity (upper panels) and absolute bolometric magnitude, $M_{\rm bol}$ (lower panels) for the zero metallicity 90-140 $M_{\odot}$ PISNe. None of these events is super-luminous and all peak luminosities are within the range of those of regular core-collapse SNe. The colors of the curves correspond to the same models as in Figure 4.

these models are as bright as typical SLSN events ($M_{\rm bol} >$ -21 mag; Gal-Yam 2012). Rotating PISNe luminosities span the whole range that is characteristic of other, regular luminosity events such as Type IIP, Type IIb/c and regular Type IIn events and can also bridge the gap between regular CC-SNe and SLSNe. Rotating PISNe of much larger mass, however, can possess peak luminosities characteristic of SLSNe (Section 4.2). A distinguishing characteristic of PISN LCs as compared to LCs of other SN events is obviously the much slower time-scales over which they evolve.

Another characteristic of PISN based upon our analysis is their intrinsically red color regardless of rotation. Figure 11 shows the $B-V$, $B-R$, $V-I$ and $V-K$ color evolution for the 90 $M_{\odot}$ and the 140 $M_{\odot}$ models. All of our models remain red in color, more so during their post-peak luminosity evolution. As expected, lower mass PISNe are redder than higher mass events. This is also in agreement with the results of Dessart et al. (2013).

4.2. *Effects of rotation and metallicity.*

As discussed in § 2.1, in order to assess the effects of rotation to the radiative properties of PISN, we have run a rapidly rotating model without the effects of the ST dynamo (140 $M_{\odot}$, no-ST) and two non-rotating models (200 $M_{\odot}$ and 260 $M_{\odot}$) all at zero metallicity. The main properties of these models are presented in Table 1.

Prior to examining how LCs and spectra compare between progenitors with different ZAMS rotation rates, we summarize the main effects of rotation on the structure of PISN progenitors discussed by Chatzopoulos & Wheeler (2012a). Rotationally–induced mixing (mainly due to meridional circulation and the ST mechanism) chemically homogenizes the star and enhances production of C, N and O. In addition, rotationally–induced mass–loss and enhanced radiatively-driven mass–loss due to the increased presence of metals in the outer layers leads to the loss of all of the H and most (or in some cases all) of the He envelope. In the case of zero rotation, we find that PISN progenitors retain both H and He and have RSG-type large radius envelopes. The CO core structures of the stars are, however, very similar regardless of the initial rotation. As a result, once the PISN sets in the nucleosynthetic products of the explosion are similar in all progenitors and the structures imported in *PHOENIX* quite similar, regardless of the initial rotation rate. The only notable differences are the increased surface abundances of C, N and O for the rotating models.

For the compact rotating PISN, the photospheric temperatures remain very high over time-scales past peak luminosity ($>$ 10,000 K) keeping H, He, C, N and O ionized. This fact, together with the intrinsically weak nature of the C and N lines, hints that we should not expect strong lines indicative of the increased C, N, O surface abundances in the model spectra of the rotating models. Figure 12 showing bolometric LCs (left panel) and peak luminosity spectra (right panel) for models of different ZAMS rotation rates confirms this assertion.

We observe that the bolometric LCs of the 90 $M_{\odot}$ and the 200 $M_{\odot}$ models and those of the 140 $M_{\odot}$ and the 260 $M_{\odot}$ models have similar peak luminosities (albeit different diffusion time-scales) and we will therefore focus our specro-

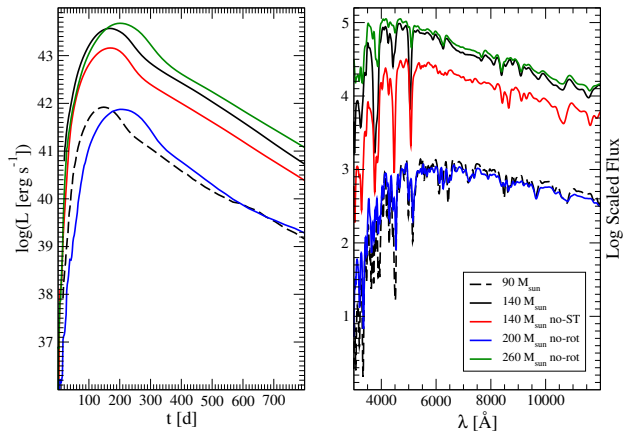

Figure 12. Bolometric LCs (left panel) and spectra (right panel) of the rapidly rotating 140 $M_\odot$ non magnetic (no-ST) model (red curve) and the non-rotating 200 and 260 $M_\odot$ models (blue and green curves respectively, § 4.2) compared to the original 90 $M_\odot$ and 140 $M_\odot$ models (solid and dashed black curves respectively).

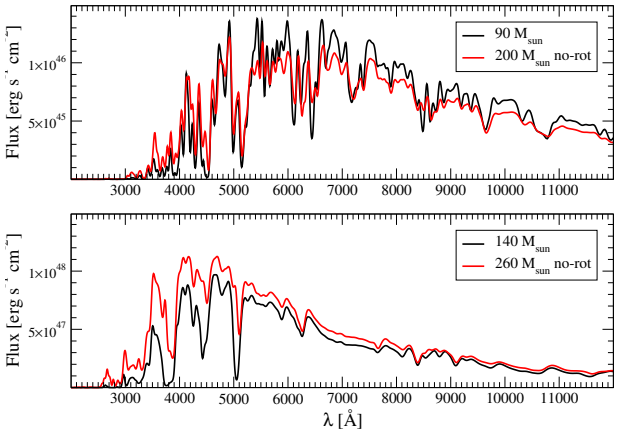

Figure 13. Peak spectrum comparisons for the 90 $M_\odot$ and the 200 $M_\odot$ no-rot (upper panel) and the 140 $M_\odot$ and the 260 $M_\odot$ (lower panel) models. The effects of pre–SN rotation do not have observable effects on the resulting spectra of PISN with similar $M_{\rm CO}$ and bolometric LC properties. The enhanced mass–loss suffered by the 90 $M_\odot$ model accounts for the more pronounced differences (mainly the O I λ 6454 Å and λ 7777 Åabsorption features).

scopic comparison efforts to these two groups of models. A more clear comparison of the peak spectra for these two sets of models is shown in the lower panel of Figure 13. The main spectral features of the 140 $M_\odot$ and 260 $M_\odot$ models are very similar considering the different peak bolometric luminosities. Strong Si, Mg and Ca features are seen in the optical with Mg and iron-group line blends strongly present in the near-UV. Regardless of the intrinsic differences in the temperature and the velocity of the expanding SN photospheres (leading to differences in the line fluxes in the 3000-5000 Åregion), there are no clear indicators of pre–SN rotation present in these spectra. The spectra at earlier phases also appear to be very similar between the two models.

In the 90 $M_\odot$ versus 200 $M_\odot$ case there are a few notable differences attributable to the pure CO core structure of the 90 $M_\odot$ PISN. Mass–loss led to the total loss of the H and He envelope for this model leaving an oxygen-rich progenitor star prior to explosion. In contrast, the outer layers of the 200 $M_\odot$ model were still H and He rich. As a result the peak luminosity spectrum of the 90 $M_\odot$ model shows stronger O I absorption features at λ 6454 Å and λ 7777 Å. These subtle differences can be more clearly distinguished in the upper panel of Figure 13. For better intuition we show the SN ejecta compositions of the rotating and non-rotating models compared in Figure 14. In can be seen that the more massive models (right panels; 140 $M_\odot$ and 260 $M_\odot$) have similar SN ejecta composition profiles regardless of rotation while the lower mass models have differences in the outer ejecta with the 90 $M_\odot$ model having an O-rich outer envelope.

The color evolution for the models of different ZAMS rotation rates discussed here is shown in Figure 15. A comparison of this figure with Figure 11 indicates that, based on the color properties alone, one cannot see a clear distinction between otherwise similar rotating and non-rotating PISN.

To infer the effects of rotation on the radiative properties of PISN, and more specifically on spectra, one has to be cautious as to not over-interpret the observations. The features in the optical part of the spectrum are more robust than the ones in the near-UV where Mg but also a variety of iron-group elements (Ti, Cr, Fe) contribute to several line-blends. Even in the case of the O I features present in the model spectrum of the 90 $M_\odot$ PISN, it would be unfounded to attribute them solely to the effects of rotation since mass–loss was the primary reason the progenitor star was mostly composed of pure oxygen. Although rotation is one avenue of mass–loss enhancement there are alternative possibilities (binary interaction, episodic/Luminous Blue Variable (LBV-type) mass–loss). Also, differences in the SN blast profiles (in terms of temperature and velocity) further increase the degeneracy between non-rotating and rotating PISN spectra. Perhaps the only qualitative difference between rotating and non-rotating models is the apparent suppression of the near-UV flux ($\lambda < 3500$ Å) attributable to the increased presence of metals in the rotating case due to the effects of pre–SN mixing. Conversely, this effect could also be due to intrisically higher metallicity, regardless of rotation (Kasen et al. 2011).

To study the effects of metallicity on the radiative properties of PISNe we have run the models 0.05 $Z_\odot$ 260 $M_\odot$, 0.1 $Z_\odot$ 300 $M_\odot$ and 0.1 $Z_\odot$ 140 $M_\odot$ as described in § 2.1 and Table 1. Figure 16 shows the resulting *PHOENIX* bolometric LCs (left panel) and spectra (right panel) as compared to our base zero metallicity 90 $M_\odot$ and 140 $M_\odot$ models. Figure 17 shows the color evolution for these higher metallicity models.

The peak luminosity spectra for rotating PISN evolved with different metallicities at ZAMS (solid black, blue and green curves in the right pane of Figure 16) all appear to be very similar with no distinguishable differences in any particular spectral features. This seems to be the case independently of phase as we illustrate in Figure 18, where the rotating zero metallicity 140 $M_\odot$ model spectra are compared with those of the 0.05 $Z_\odot$ 260 $M_\odot$ model at the same phases (before, during and after peak luminosity).

In contrast, for the 140 $M_\odot$ models for which a metal content corresponding to 0.1 $Z_\odot$ was added prior to import to *FLASH* ("pF" model; dashed red curve) and *PHOENIX* ("pP" model; solid red curve) differences are seen in the near-UV spectral flux and Ca H&K absorption. For details on these

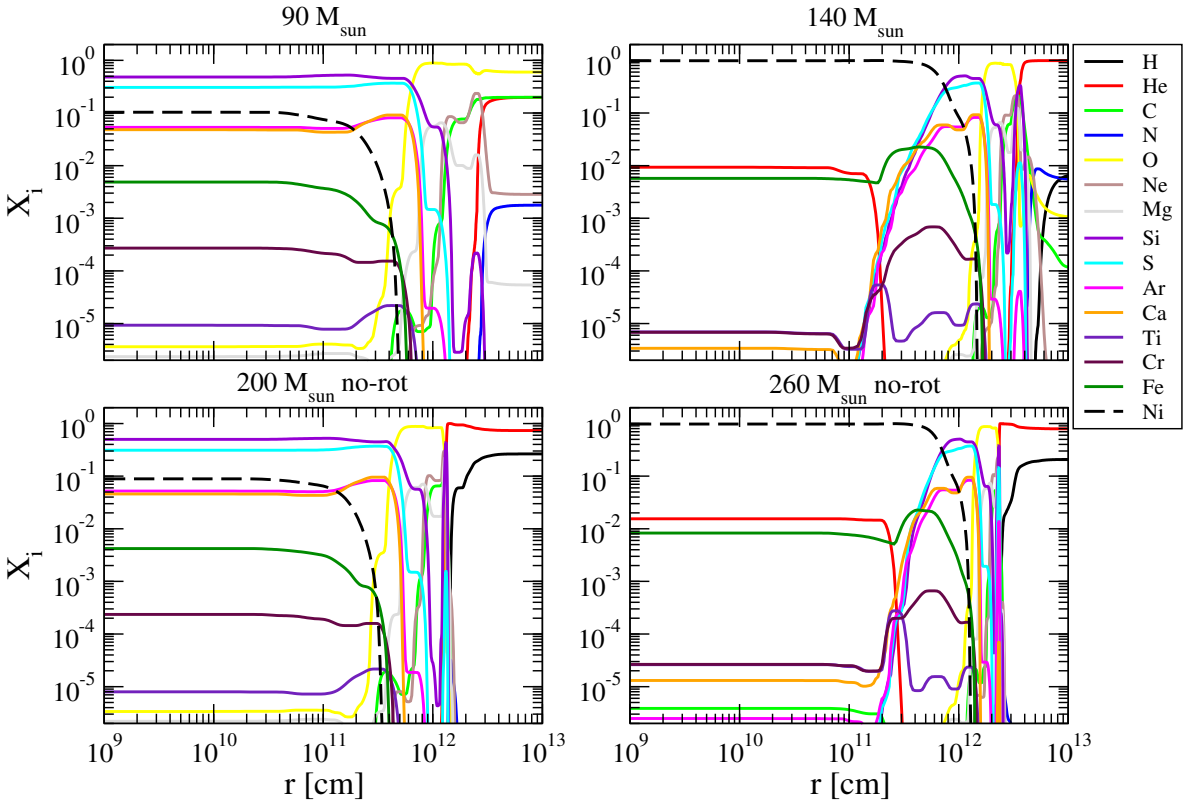

Figure 14. Comparison of the pre-SN compositions of the rotating 90 $M_\odot$ and 140 $M_\odot$ models (upper panels) against the non-rotating 200 $M_\odot$ and 260 $M_\odot$ models (lower panels) that produce similar bolometric LCs (Fig 12).

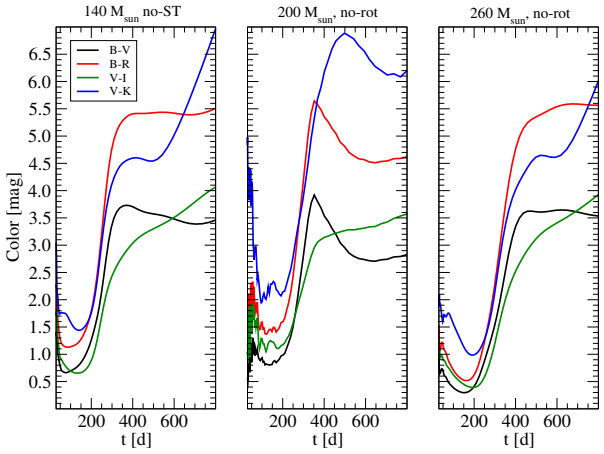

Figure 15. Evolution of the $B-V$, $B-R$, $V-I$ and $V-K$ colors for the 140 $M_\odot$ non-magnetic (no-ST; left panel), the 200 $M_\odot$ no-rot (middle panel) and the 260 $M_\odot$ no-rot (right panel) model (§ 4.2).

models refer back to the discussion in § 2.1. More specifically, the near-UV flux is suppressed in the "pP" model as compared to the original 140 $M_\odot$ model. The "pF" model also shows a much smaller far UV flux suppression at $\lambda < 4500$ Å while for the most part the spectrum is identical to the original 140 $M_\odot$ model. The flux deficit is more dramatic in the "pP" case where the metallicity was added prior to calculating the *PHOENIX* spectra. This is because once the PISN explosion occur, the bulk of the additional metal content in the core of the progenitor contributes to the formation of ^{56}Ni and other iron-group elements through nuclear burning. By the time the SN photosphere expands, the blast profile is very similar to that of the 140 $M_\odot$ model. In other words, the progenitor metallicity information is undecipherable in the post-explosion PISN spectra.

This is an important point of contrast with the results of (Kasen et al. 2011) illustrated in their Figure 11. They too find that increased metallicity has the effect to reduce the UV flux for otherwise identical PISN progenitors, but they also add the metal content immediately prior to doing the *SEDONA* radiative transfer calculations. Self-consistent evolution of PISNe with higher metal content from the ZAMS or even addition of extra metal abundances to a model prior to the explosion does not lead to significant differences in the spectra of our rotating models as compared to zero or low-metallicity models. Note that, as we discuss in Section 4.3, our PISN models compare well with the (Kasen et al. 2011) models of the same ZAMS metallicity.

The radiative properties of PISNe appear to be degenerate across differences in ZAMS rotation rate and metallicity and seem to depend more on basic SN blast profile properties such as the temperature and velocity of the SN ejecta. Once the explosion sets in, the products of nuclear burning are predominantly IMEs in the outer and iron-peak elements in the inner ejecta. Even the detailed spectral evolution of PISNe appears to be quite similar for models of different initial conditions. Pre-SN surface composition, on the other hand, seems to be the only factor leading to robust differences in the PISN spectra, as showcased by the 90 $M_\odot$ model discussed above. Dif-

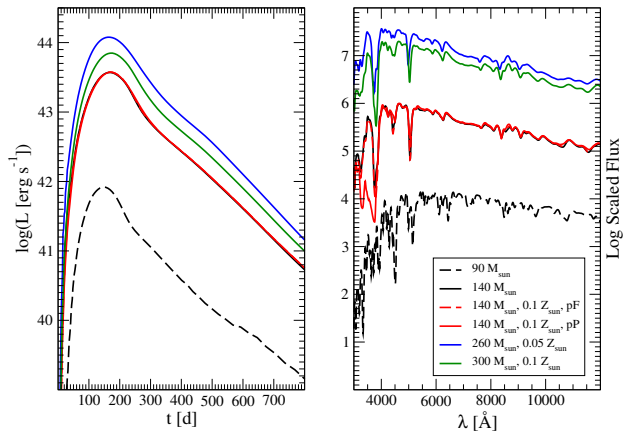

Figure 16. Bolometric LCs (left panel) and spectra (right panel) of the 0.1 $Z_\odot$ 140 $M_\odot$ model prior to import to *FLASH* ("pF"; dashed red curve) and *PHOENIX* ("pP"; solid red curve), the 0.05 $Z_\odot$ 260 $M_\odot$ and the 0.1 $Z_\odot$ 300 $M_\odot$ model (blue and green curves respectively) compared to the original 90 $M_\odot$ and 140 $M_\odot$ models (solid and dashed black curves respectively). Evolution with different initial metallicity does not change the resulting PISN spectra significantly. Artifical addition of metal content prior to the radiative transfer calculation leads to the suppression of UV flux (model "pP").

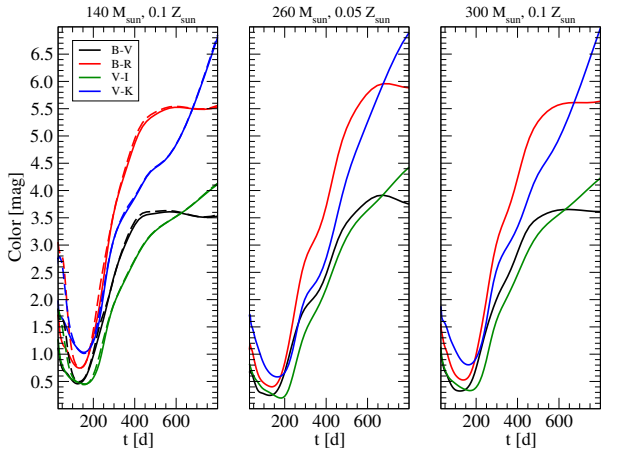

Figure 17. Evolution of the $B-V$, $B-R$, $V-I$ and $V-K$ colors for the 0.1 $Z_\odot$ 140 $M_\odot$ (left panel), the 0.05 $Z_\odot$ 200 $M_\odot$ (middle panel) and the 0.1 $Z_\odot$ 300 $M_\odot$ (right panel) model (see Section 4.2). The dashed curves in the left panel correspond to the 140 $M_\odot$ "pP" model.

ferences in pre–SN composition are primarily attributable to the extent of mass–loss suffered by the progenitor. As such, H/He-poor PISNe can be distinguished by the presence of O I absorption features in the optical, and that only if the appropriate temperature conditions are maintained in the SN ejecta.

4.3. *Comparison with other PISN studies.*

The LCs and color evolution we find for rotating PISNe have similar broad, qualitative properties with the non–LTE LCs of the non-rotating models studied by Kasen et al. (2011) and Dessart et al. (2013). To compare with these studies, we use our brightest zero metallicity PISN model (140 $M_\odot$). This model is the closest to the bare "helium" star He100 models of both Kasen et al. (2011) (He100K) and Dessart et al. (2013)

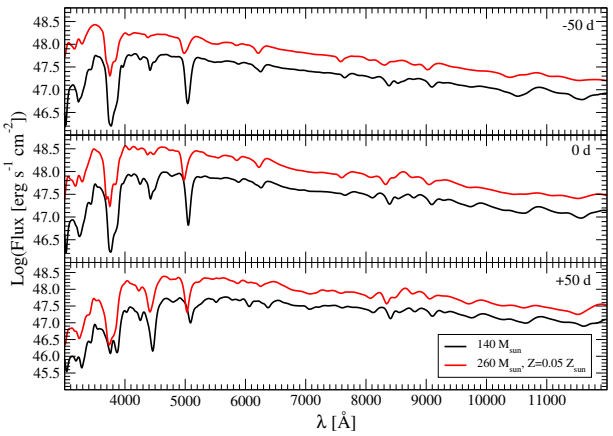

Figure 18. Comparison of the 140 $M_\odot$ and the 0.05 $Z_\odot$ 260 $M_\odot$ model spectra at the contemporaneous epochs of -50 d (upper panel), 0 d (middle panel) and +50 d (lower panel) with respect to peak luminosity. There are no significant differences induced by different ZAMS metallicity in the spectral evolution of otherwise similar PISNe.

(He100D) in terms of $M_{\rm CO}$, $M_{\rm Ni}$ and final structural properties modulo differences in the surface abundances of C, N and O that are enhanced in our model due to the effects of rotationally-induced mixing.

The bolometric LC of our 140 $M_\odot$ model is very close in terms of both peak luminosity ($M_{\rm bol,peak}$ = -20.2 mag, $L_{peak} \simeq 4 \times 10^{43}$ erg) and rise time to maximum ($t_{peak} \simeq 170$ d) with the He100K and He100D models. The same holds for the broad band LCs: the same behavior is seen in all three studies going from the bluer (U) to the redder (K) band. An exception is the range of peak filter magnitudes where our model is more in agreement with He100D than with He100K who find a larger range ($\sim$ -19 $<$ M $<$ -26 from $U_{\rm peak}$ to $K_{\rm peak}$). The peak absolute V magnitudes recovered from all three studies are in good agreement ($M_V \sim$ -20.5 to -21) regarding the differences in the initial progenitors. The color evolution of the 140 $M_\odot$ model is qualitatively similar to that of the He100D model, although we find it to be consistently redder for the rotating PISN. This could be due to differences between our LTE treatment and the Dessart et al. (2013) non–LTE approach.

A comparison of the spectral evolution between the three studies reveals several similarities as well. In terms of the peak luminosity spectrum, the strongest features seem to be recovered by all three approaches, somewhat resembling Type Ic SN spectra. More specifically the strong Mg I, Mg II, Si II, Ca II and O I lines are recovered by all studies. Figure 19 shows a comparison of the 140 $M_\odot$ spectra for different phases with respect to peak luminosity and the He100K peak spectrum.

Given the intrinsic differences of the progenitors, the agreement between the spectra of the 140 $M_\odot$ model and He100K is very good in the optical (Figure 19). Obvious differences do exist in some near-IR features ($\lambda > 8300$ Å) and the near-UV flux. We wish to note that besides examining the radiative properties of PISN this excercise also serves as direct comparison of model PISN spectra obtained from different codes. It is remarkable that given differences in the numerical treatment of radiative transfer between *PHOENIX* and *SEDONA* (that uses a Monte Carlo method) the main PISN spectro-

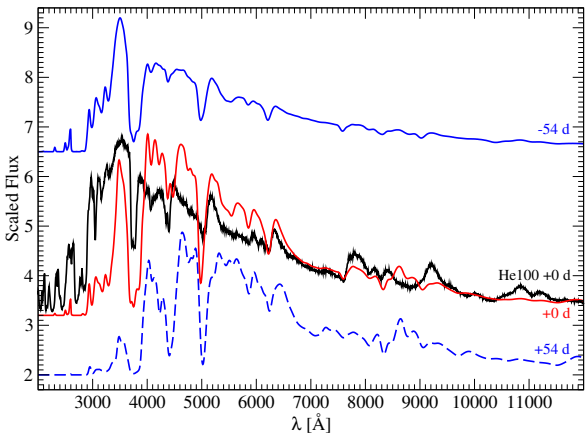

Figure 19. Comparison of the Kasen et al. (2011) He100 peak luminosity spectrum (black curve) with the -54 d, +54 d (solid and dashed blue curve respectively) and peak luminosity (red curve) spectra of the 140 $M_{\odot}$ model.

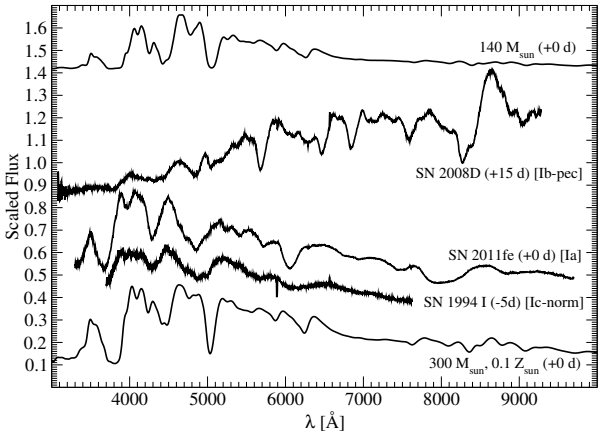

Figure 20. Comparison of the 140 $M_{\odot}$ and the 300 $M_{\odot}$ ($Z = 0.1\ Z_{\odot}$) rotating PISN model spectra at peak luminosity with observed spectra of the the normal Type Ic SN 1994I (Filippenko et al. 1995), the Type Ia SN 2011fe (Nugent et al. 2011) and the peculiar Type Ib SN 2008D (Modjaz et al. 2009). The parentheses indicate the phase after peak luminosity in days and the brackets the SN type. All the observed SN spectra were downloaded from the Weizmann Interactive Supernova Data Repository (*WISeREP*; Yaron & Gal-Yam 2012).

scopic characteristics recovered are in good agreement.

4.4. *Comparison with observations.*

Given the main properties of model PISN spectra that we have discussed in this work, it remains to examine if such events have been actually observed. At first glance, the general appearance of model PISN spectra appears to qualitatively resemble Type Ia and some normal Type Ic SN events with the lack of apparent H and He features and a strong presence of metals such as O, Mg, Si and Ca. We attempt to illustrate these similarities in Figure 20 where we plot the peak luminosity 140 $M_{\odot}$ and 0.1 $Z_{\odot}$ 300 $M_{\odot}$ spectra against near-maximum spectra of SN 2008D (Type Ib), SN 2011fe (Type Ia) and SN 1994I (Type Ic). Obviously, SN 2008D is a bad match (also given the absence of He in our model spectra) but the other two events exhibit some similarities with model 0.1 $Z_{\odot}$ 300 $M_{\odot}$.

With regards to the proposed association between PISNe and a few observed SLSN events (Gal-Yam et al. 2009), we find that the emission properties of PISNe are quite different from those of the proposed candidate SN 2007bi, in agreement with the results of Dessart et al. (2013). In particular, we find that PISNe of several metallicities and rotation rates are intrinsically red events and, in most cases, do not produce super-luminous events due to the severe mass–loss suffered during the progenitor evolution. This is due to the fact that PISNe tend to have lower $M_{\rm Ni}/M_{\rm f}$ ratios than Type Ia or Type Ic-norm events leading to slowly evolving LCs with peak luminosities that span a large range from sub-luminous to some super-luminous events in the most extreme cases. For very high ZAMS mass ($> 200\ M_{\odot}$), several solar masses of ^{56}Ni are produced powering a super-luminous explosion. From the suite of models considered in our work with metallicities in agreement with that of the host of SN 2007bi, the only two that reach peak luminosities comparable to those of the event are the 0.1 $Z_{\odot}$ 300 $M_{\odot}$ and the 0.05 $Z_{\odot}$ 260 $M_{\odot}$ models. The observed R-band LC of SN 2007bi is compared against the LCs of these two models in Figure 21.

Based only on the LC, it can be deduced that a rotating PISN with $Z \simeq 0.05$-$0.1\ Z_{\odot}$ is indeed a good model for SN 2007bi; however, a closer look at the spectral and color evolution of this event as compared with the model

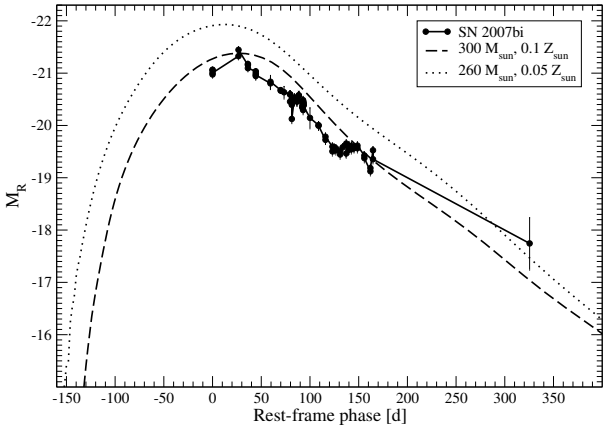

Figure 21. The observed R-band LC of SN 2007bi (Gal-Yam et al. 2009) (solid curve) compared to the R-band model LCs of of the rotating 0.1 $Z_{\odot}$ 300 $M_{\odot}$ (dashed curve) and 0.05 $Z_{\odot}$ 260 $M_{\odot}$ (dotted curve) models. Although PISN model LCs seem to be a good match to the observed LCs of some SLSNe, such as SN 2007bi, the predicted spectral evolution is remarkably different than the one observed.

predictions reveals certain inconsistencies. The most important disagreement stems from a careful comparison of the model PISN spectra with those of SN 2007bi at contemporaneous epochs. This is an issue originally raised by Dessart et al. (2013) with regards to the apparent spectral agreement found between model He100K and the observed +54 d post-maximum spectrum of SN 2007bi by Kasen et al. (2011). The agreement was due to the fact that the He100K spectrum compared with the data was one at 50 d before peak, at an epoch when the PISN was still hot and blue. At later, post-maximum epochs, when the spectra of SN 2007bi were obtained, the model PISN spectra are much redder and strongly line-blanketed. A caveat to performing nearly-contemporaneous model to data spectral comparisons is the

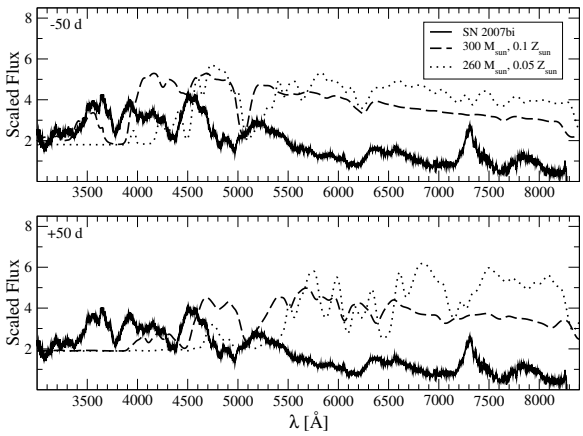

Figure 22. Comparison of the spectrum of SN 2007bi at +54d (Gal-Yam et al. 2009) (solid curve) with that of the 0.1 $Z_{\odot}$ 300 $M_{\odot}$ (dashed curve) and the 0.05 $Z_{\odot}$ 260 $M_{\odot}$ (dotted curve) model at -50 d (upper panel) and +50 d (lower panel) with respect to peak luminosity.

fact that for many SLSN events, including SN 2007bi, the exact explosion date and therefore the phase of the observed spectrum are quite uncertain, as noted by Chatzopoulos et al. (2013b). Nevertheless, to be consistent with the other authors, we will also accept the phase of the earliest observed SN 2007bi spectrum to be +54 d after peak luminosity.

Figure 22 shows the -50 d and +50 d (with regards to peak luminosity) spectra of the rotating 0.05 $Z_{\odot}$ 260 $M_{\odot}$ and 0.1 $Z_{\odot}$ 300 $M_{\odot}$ models compared with the observed spectrum of SN 2007bi +54 d after peak luminosity.

The comparison at the nearly contemporaneous epoch of +50 d (lower panel of Figure 22) reveals that the PISN models possess continua that are much redder and with different spectral features than the observations of SN 2007bi suggest. The agreement between the earlier model spectrum of the 0.1 $Z_{\odot}$ 300 $M_{\odot}$ model (-50 d) and the data is slightly better but yet not nearly strong enough to suggest a physically consistent connection to the PISN mechanism. The color evolution of the model PISN spectra further affirms the fact that SN 2007bi was not a PISN. SN 2007bi retained blue color and a hot continuum for a long time after peak suggesting that a different, more efficient SN ejecta heating mechanism was at play and for a longer time-scale than the radioactive decay of ^{56}Ni. Potential alternative candidates are magneto-rotational energy injection due to the spin-down of a young magnetar (Dessart et al. 2012) and H-poor SN ejecta - CSM interaction (Chatzopoulos & Wheeler 2012b; Chatzopoulos et al. 2013b). More detailed radiation hydrodynamics and non–LTE radiative transfer modelling is required to clearly identify the power-input mechanism for SN 2007bi and other H-poor SLSN (SLSN-I).

5. DISCUSSION AND CONCLUSIONS

In this paper we explored the radiative emission properties of model PISNe for a variety of progenitors of different ZAMS mass (90-300 $M_{\odot}$), metallicity (0-0.1 $Z_{\odot}$) and rotation rate. The analysis we performed was done in three basic stages: stellar evolution from ZAMS up to pre–SN with *MESA*, nuclear burning and hydrodynamic evolution of the explosion phase up to post SN shock break out with *FLASH* and radiative transfer with *PHOENIX* yielding the final model spectra and LCs. For a subset of our models (the zero metallicity rotating 90-140 $M_{\odot}$ models) an additional step included the mapping of the pre-SBO profiles to the radiation hydrodynamics code *RAGE* where the phase of SN shock breakout and the corresponding LCs and SEDs were computed.

As has been discussed in past studies (Chatzopoulos & Wheeler 2012a; Yoon et al. 2012) the main effects of rotation on the evolution of PISN progenitors is the enhanced mixing leading to the formation of larger CO cores for initially smaller ZAMS mass as compared to the case of zero rotation, and the increased mass–loss suffered leading to bare CO stars with little or no He in their envelopes prior to explosion. As such, the pre-explosion zero metallicity models we consider here were compact ($R_{\rm f} < 2 \times 10^{11}$ cm) and dense all the way to the surface. The *RAGE* simulations revealed that the SBO SEDs of these events are significantly hotter than those implied for RSG and BSG progenitors (Kasen et al. 2011) peaking in the hard X-rays (1-100 keV). Nevertheless, the combination of lower pre–SN radii, higher SN ejecta temperatures and velocities and harder emission leads to SBO bolometric LCs with peaks similar to those found for RSG and BSG progenitors (10^{45}-10^{46} erg s^{-1}).

The main, long-duration part of the LCs powered by the radioactive decays of ^{56}Ni and ^{56}Co was studied for all models using the *PHOENIX* results. For most PISN models, the implied $M_{\rm Ni}/M_{\rm ej}$ ratios were below 10 %, a value close to Type IIP events leading to intrinsically red colors, as noted by Dessart et al. (2012). As such, most PISN exhibited peak luminosities spanning the range observed for normal Type II and Ib/c events. Super-luminous LCs were found only in the most massive non-zero metallicity 260 $M_{\odot}$ and 300 $M_{\odot}$ models. We stress that super-luminous PISN LCs are possible for zero metallicity models with higher masses than the ones we studied in this work ($>$ 140 $M_{\odot}$). Nevertheles, all models evolved with redder colors than those observed for SLSN-I and, more specifically, SN 2007bi.

We investigated the potential to distinguish rotation and metallicity information from the observed PISN spectra and came to the conclusion that the spectroscopic properties of these events are quite degenerate and any attempt to uncover them based on observed spectra would be highly uncertain. More specifically, we find that the increased abundances of C, N and O in the outer layers of the rotating models do not have a significant effect in the spectra and that, once the explosion sets-in the products of nuclear burning are the same regardless of the pre–SN rotational mixing and metallicity. The peak luminosity spectra, but also the spectral evolution of PISN in general, appear to be quite similar across different initial metallicity and rotation rate. This is in contradiction with the result of Kasen et al. (2011) that increased metallicity leads to suppressed near-UV flux and differences in some spectral features. This difference is attributable to the fact that in their approach the extra metals were added after the PISN explosion and prior to the free expansion phase where the radiative transfer calculation is done. Self-consistent evolution of PISN with ZAMS metallicity results in final spectra with similar properties.

Most of the spectroscopic properties across the PISN parameter space arise due to fundamental differences in pre–SN composition and different SN ejecta masses, temperatures and velocities. The more massive models have a somewhat bluer continuum with fewer lines in the optical than then less massive ones. These points are well illustrated by our 90 $M_{\odot}$ model that was a pure oxygen star prior to explosion. The

oxygen-rich composition together with the high SN ejecta temperature leads to spectra with strong O I absorption features that are distinguishable from those of the other models.

Our model PISN spectra compare well against those calculated by Kasen et al. (2011) and Dessart et al. (2013) for similar progenitors (more specifically their bare 100 $M_{\odot}$ He core model He100). This confirms that regardless of the differences in numerical methods between different codes and LTE versus non–LTE treatment the results for the main emission characteristics of PISN are consistent.

Although the R-band LC of the 0.1 $Z_{\odot}$ 300 $M_{\odot}$ model reproduces the main features of the LC of SN 2007bi, it is not sufficient information to categorize the event as a PISN. Comparison of our model spectra against the observed +54 d spectrum of the super-luminous SN 2007bi at contemporaneous epochs confirms that SN 2007bi was not a PISN, in agreement with the result of Dessart et al. (2013). More specifically, PISNe appear to have redder color evolution and different spectroscopic features compared to all observed SLSNe. This could be due to the fact that most SLSNe have been observed in environments with metallicities $\sim 0.45\ Z_{\odot}$ (Lunnan et al. 2014) disfavoring the formation of very massive pre–SN CO cores due to strong mass–loss. This value is near the upper limit metallicity of 1/3 $Z_{\odot}$ for the most massive progenitors assuming standard initial mass functions (IMF) (Langer et al. 2007). In addition, other models of PISN present in the literature with LCs in agreement with that of SN 2007bi have adopted a progenitor metallicity that is far lower than that of the host galaxy of the event (Kozyreva et al. 2014) or have made simplifying assumptions with regards to the progenitor mass–loss history (Kasen et al. 2008; Gal-Yam et al. 2009). Given these results, we conclude that all SLSN events observed so far must be powered via alternative mechanisms with the most promising candidates being radiation from a mangetar-spin down (Dessart et al. 2012; McCrum et al. 2014) and CSM interaction of the H-rich and H-poor variety (Chatzopoulos & Wheeler 2012b; Chatzopoulos et al. 2013b; Benetti et al. 2014; Nicholl et al. 2014).

The PISN phenomenon is expected to be more prevalent in ultra-low and zero metallicity environments appropriate to the conditions of the early Universe. Some Population III star-formation simulations predict the first stars to be massive and rotating (Stacy et al. 2012, 2013), well within the PISN parameter space. As such, the future of observational research in the subject seems to rest on the shoulders of exciting upcoming missions such as *WFIRST* and *JWST*.

We would like to thank Wesley Even, Sean M. Couch, Donald Q. Lamb, Ryan Chornock, Ken Chen, Alexandra Kozyreva and Ragnhild Lunnan for useful discussions and comments. This work was supported in part by the STScI grants AR 12820 and 13276 and the National Science Foundation under grants AST-0909132 and PHY-0822648 for the Physics Frontier Center "Joint Institute for Nuclear Astrophysics" (JINA). EC would like to thank the Enrico Fermi Institute for its support via the Enrico Fermi Fellowship. D.J.W. was supported by the European Research Council under the European Community's Seventh Framework Programme (FP7/2007 - 2013) via the ERC Advanced Grant "STARLIGHT: Formation of the First Stars" (project number 339177).

REFERENCES

Abel, T., Anninos, P., Norman, M. L., & Zhang, Y. 1998, ApJ, 508, 518, astro-ph/9705131
Barkat, Z., Rakavy, G., & Sack, N. 1967, Physical Review Letters, 18, 379
Benetti, S. et al. 2014, MNRAS, 441, 289, 1310.1311
Bromm, V., Coppi, P. S., & Larson, R. B. 2002, ApJ, 564, 23, astro-ph/0102503
Bromm, V., & Larson, R. B. 2004, ARAA, 42, 79, astro-ph/0311019
Bromm, V., Yoshida, N., Hernquist, L., & McKee, C. F. 2009, Nature, 459, 49, 0905.0929
Brott, I. et al. 2011a, A&A, 530, A115, 1102.0530
——. 2011b, A&A, 530, A116, 1102.0766
Chatzopoulos, E., & Wheeler, J. C. 2012a, ApJ, 748, 42, 1201.1328
——. 2012b, ApJ, 760, 154, 1210.1617
Chatzopoulos, E., Wheeler, J. C., & Couch, S. M. 2013a, ApJ, 776, 129, 1308.4660
Chatzopoulos, E., Wheeler, J. C., Vinko, J., Horvath, Z. L., & Nagy, A. 2013b, ApJ, 773, 76, 1306.3447
Chatzopoulos, E. et al. 2011, ApJ, 729, 143, 1101.3581
Chen, K.-J., Heger, A., Woosley, S., Almgren, A., & Whalen, D. 2014a, ArXiv e-prints, 1402.5960
Chen, K.-J., Woosley, S., Heger, A., Almgren, A., & Whalen, D. 2014b, ArXiv e-prints, 1402.4134
Crowther, P. A., Schnurr, O., Hirschi, R., Yusof, N., Parker, R. J., Goodwin, S. P., & Kassim, H. A. 2010, MNRAS, 408, 731, 1007.3284
de Souza, R. S., Ishida, E. E. O., Whalen, D. J., Johnson, J. L., & Ferrara, A. 2014, MNRAS, 442, 1640, 1401.2995
Dessart, L., Hillier, D. J., Waldman, R., Livne, E., & Blondin, S. 2012, MNRAS, 426, L76, 1208.1214
Dessart, L., Waldman, R., Livne, E., Hillier, D. J., & Blondin, S. 2013, MNRAS, 428, 3227, 1210.6163
Dubey, A., Reid, L. B., Weide, K., Antypas, K., Ganapathy, M. K., Riley, K., Sheeler, D., & Siegal, A. 2009, ArXiv e-prints, 0903.4875
Dufton, P. L. et al. 2011, ApJL, 743, L22, 1111.0157
Ekström, S. et al. 2012, A&A, 537, A146, 1110.5049
Ekström, S., Meynet, G., Chiappini, C., Hirschi, R., & Maeder, A. 2008, A&A, 489, 685, 0807.0573
Filippenko, A. V. et al. 1995, ApJL, 450, L11
Frey, L. H., Even, W., Whalen, D. J., Fryer, C. L., Hungerford, A. L., Fontes, C. J., & Colgan, J. 2013, ApJS, 204, 16, 1203.5832
Fryxell, B. et al. 2000, ApJS, 131, 273
Gal-Yam, A. 2012, Science, 337, 927, 1208.3217
Gal-Yam, A. et al. 2009, Nature, 462, 624, 1001.1156
Gittings, M. et al. 2008, Computational Science and Discovery, 1, 015005, 0804.1394
Glover, S. 2013, in Astrophysics and Space Science Library, Vol. 396, Astrophysics and Space Science Library, ed. T. Wiklind, B. Mobasher, & V. Bromm, 103, 1209.2509
Greif, T. H., Springel, V., White, S. D. M., Glover, S. C. O., Clark, P. C., Smith, R. J., Klessen, R. S., & Bromm, V. 2011, ApJ, 737, 75, 1101.5491
Hachinger, S. et al. 2013, MNRAS, 429, 2228, 1208.1267
Hauschildt, P. H. 1992, J. Quant. Spec. Radiat. Transf., 47, 433
Hauschildt, P. H., & Baron, E. 1999, Journal of Computational and Applied Mathematics, 109, 41, astro-ph/9808182
——. 2004, A&A, 417, 317, astro-ph/0401164
Heger, A., Langer, N., & Woosley, S. E. 2000, ApJ, 528, 368, astro-ph/9904132
Heger, A., & Woosley, S. E. 2002, ApJ, 567, 532, astro-ph/0107037
Hillier, D. J., & Dessart, L. 2012, MNRAS, 424, 252, 1204.0527
Hummel, J. A., Pawlik, A. H., Milosavljević, M., & Bromm, V. 2012, ApJ, 755, 72, 1112.5207
Joggerst, C. C., & Whalen, D. J. 2011, ApJ, 728, 129, 1010.4360
Kasen, D., & Bildsten, L. 2010, ApJ, 717, 245, 0911.0680
Kasen, D., Heger, A., & Woosley, S. 2008, in American Institute of Physics Conference Series, Vol. 990, First Stars III, ed. B. W. O'Shea & A. Heger, 263–267
Kasen, D., Woosley, S. E., & Heger, A. 2011, ApJ, 734, 102, 1101.3336
Kozyreva, A., Blinnikov, S., Langer, N., & Yoon, S.-C. 2014, A&A, 565, A70, 1403.5212
Langer, N., Norman, C. A., de Koter, A., Vink, J. S., Cantiello, M., & Yoon, S.-C. 2007, A&A, 475, L19, 0708.1970
Lucy, L. B. 1991, ApJ, 383, 308
Lunnan, R. et al. 2014, ApJ, 787, 138, 1311.0026
Maeder, A., & Meynet, G. 2011, ArXiv e-prints, 1109.6171
McCrum, M. et al. 2014, MNRAS, 437, 656, 1310.4417
Modjaz, M. et al. 2009, ApJ, 702, 226, 0805.2201
Moriya, T. J., Blinnikov, S. I., Tominaga, N., Yoshida, N., Tanaka, M., Maeda, K., & Nomoto, K. 2013, MNRAS, 428, 1020, 1204.6109
Moriya, T. J., & Tominaga, N. 2012, ApJ, 747, 118, 1110.3807
Nicholl, M. et al. 2014, ArXiv e-prints, 1405.1325
Nugent, P. E. et al. 2011, Nature, 480, 344, 1110.6201
Ober, W. W., El Eid, M. F., & Fricke, K. J. 1983, A&A, 119, 61
Olson, G. L., & Kunasz, P. B. 1987, J. Quant. Spec. Radiat. Transf., 38, 325
Pan, T., Kasen, D., & Loeb, A. 2012, MNRAS, 422, 2701, 1112.2710
Paxton, B., Bildsten, L., Dotter, A., Herwig, F., Lesaffre, P., & Timmes, F. 2011, ApJS, 192, 3, 1009.1622
Paxton, B. et al. 2013, ApJS, 208, 4, 1301.0319

Quimby, R. M., Aldering, G., Wheeler, J. C., Höflich, P., Akerlof, C. W., & Rykoff, E. S. 2007, ApJL, 668, L99, 0709.0302
Rakavy, G., & Shaviv, G. 1967, ApJ, 148, 803
Rakavy, G., Shaviv, G., & Zinamon, Z. 1967, ApJ, 150, 131
Scannapieco, E., Madau, P., Woosley, S., Heger, A., & Ferrara, A. 2005, ApJ, 633, 1031, astro-ph/0507182
Smith, N. et al. 2007, ApJ, 666, 1116, astro-ph/0612617
Smith, N., & McCray, R. 2007, ApJL, 671, L17, 0710.3428
Spruit, H. C. 1999, A&A, 349, 189, astro-ph/9907138
——. 2002, A&A, 381, 923, astro-ph/0108207
Stacy, A., Greif, T. H., & Bromm, V. 2012, MNRAS, 422, 290, 1109.3147
Stacy, A., Greif, T. H., Klessen, R. S., Bromm, V., & Loeb, A. 2013, MNRAS, 431, 1470, 1209.1439
Stoll, R., Prieto, J. L., Stanek, K. Z., & Pogge, R. W. 2013, ApJ, 773, 12, 1205.2338
van Rossum, D. R. 2012a, ApJ, 756, 31, 1206.5463
——. 2012b, ArXiv e-prints, 1208.3781
Whalen, D. J. 2013, Acta Polytechnica, 53, 573, 1209.4688
Whalen, D. J. et al. 2013a, ApJ, 777, 110, 1211.4979
Whalen, D. J., Fryer, C. L., Holz, D. E., Heger, A., Woosley, S. E., Stiavelli, M., Even, W., & Frey, L. H. 2013b, ApJL, 762, L6, 1209.3457
Woosley, S. E. 2010, ApJL, 719, L204, 0911.0698
Woosley, S. E., Blinnikov, S., & Heger, A. 2007, Nature, 450, 390, 0710.3314
Yaron, O., & Gal-Yam, A. 2012, PASP, 124, 668, 1204.1891
Yoon, S.-C., Dierks, A., & Langer, N. 2012, A&A, 542, A113, 1201.2364
Yoon, S.-C., & Langer, N. 2005, A&A, 443, 643, astro-ph/0508242
Yusof, N. et al. 2013, MNRAS, 433, 1114, 1305.2099